Intense upper ocean mixing due to large aggregations of spawning fish

Bieito Fernández Castro[1,2], Marian Peña[3], Enrique Nogueira[4], Miguel Gilcoto[2], Esperanza Broullón[5], Antonio Comesaña[5], Damien Bouffard[6], Alberto C. Naveira Garabato[1] & Beatriz Mouriño-Carballido[5]

[1]*Ocean and Earth Science, National Oceanography Centre, University of Southampton, Southampton, UK*

[2]*Departamento de Oceanografía, Instituto de Investigacións Mariñas (IIM-CSIC), Vigo, Spain*

[3]*Centro Oceanográfico de Baleares (IEO, CSIC), Palma de Mallorca, Spain*

[4]*Centro Oceanográfico de Vigo (IEO, CSIC), Vigo, Spain*

[5]*Centro de Investigación Mariña, Universidade de Vigo, GOB, Vigo, Spain*

[6]*Eawag, Surface Waters – Research and Management, Swiss Federal Institute of Aquatic Science and Technology, Kastanienbaum, Switzerland*

Small-scale turbulent mixing plays a pivotal role in shaping the circulation and a broad range of physical and biogeochemical ocean processes. Despite advances in understanding geophysical processes responsible for this mixing, the nature and importance of biomixing – turbulent mixing caused by marine biota – remains controversial. A major source of uncertainty pertains to the efficiency of biomixing – the fraction of the turbulent energy produced through swimming that is spent in mixing the ocean vertically –, which the few *in situ* observations available suggest to be much lower than that of geophysical turbulence. Here, we shed light on this problem by analysing 14 days of continuous measurements of centimetre-scale turbulence in a coastal upwelling area. We show that turbulent dissipation is elevated 10 to 100-fold (reaching 10^{-6}-10^{-5} W kg^{-1}) every night during due to the swimming activity of large aggregations of anchovies that gather regularly over the spawning season. Turbulent mixing is invigorated concurrently to dissipation, and occurs with an efficiency comparable

to that of geophysical turbulence. Our results demonstrate that biologically-driven turbulence can be a highly effective mixing agent, and call for a re-examination of its impacts on productive upper-ocean regions.

Turbulence is a fundamental component of the ocean's energy budget, for it mediates the transfer of kinetic energy from large (1-1000 km) to small (0.1-1 cm) scales, where such energy is dissipated as heat by molecular viscosity[1]. However, dissipation is just one of two possible fates of turbulent kinetic energy (TKE). As turbulent motions stir the water column, microscale physical and chemical gradients are generated and ultimately eroded by molecular diffusion, thereby resulting in mixing. When acting on a stable density profile, such as the oceanic pycnocline, turbulent mixing drives an upward transport of mass, and hence transforms a fraction of the TKE into potential energy[2]. This fraction, referred to as mixing efficiency, is relatively uncertain and challenging to quantify *in situ*. Observations and idealized simulations indicate that the mixing efficiency often approaches a value of ~0.16 (refs.3, 4), as is characteristic of shear instabilities (a major source of ocean turbulence[5,6]), yet there is mounting evidence that the mixing efficiency may vary extensively[7].

The debate surrounding mixing efficiency is particularly relevant for appraising the significance of biomixing[8]. Although winds and tides undeniably constitute the major sources of energy for ocean mixing on a global scale[9], it has been suggested[10,11] that swimming organisms (from zooplankton to fish and marine mammals) may also contribute a substantial energy input[12], at least on regional scales[13]. The relevance of this suggestion was initially endorsed by dynamical[13] and metabolic[14] considerations, laboratory experiments[15], and early observations of elevated TKE dissipation ($\sim 10^{-5}$ W kg^{-1}) in fish aggregations[16] and migrating krill swarms[17]. However, subsequent studies found biophysical turbulence extremely challenging to capture in lakes and oceans, indicating that this phenomenon might be rarer than originally thought[18–22]. Further, what little evidence exists of mixing produced by biophysical turbulence suggests that the mixing efficiency of such

turbulence is very low (<0.01) relative to that of geophysical, shear-driven turbulence. This evidence is based on the concurrent measurement of the rates of dissipation of TKE (ε, a measure of the intensity of turbulence) and of thermal variance (χ, a measure of the intensity of mixing) –respectively quantified from observations of centimetre-scale velocity and temperature gradients– in the presence of swimming organisms[16,20,22–24]. Only two of these investigations reported high ε levels within fish aggregations[23,24] but, in both cases, these were associated with low values of χ, i.e. weak mixing. Thus, the present balance of evidence points toward dismissing the old-proposed view of a significant large-scale influence of biomixing.

Here, we contest and redress this balance by demonstrating the occurrence of recurrent, intense and efficient biomixing in an embayment affected by wind-driven coastal upwelling pulses (Ría de Pontevedra, NW Iberia, Extended Data Figure 1)[25,26]. This demonstration rests on the analysis of a two-week data set of highly (temporally and vertically) resolved observations of hydrographic properties, turbulent dissipation and mixing rates, and acoustic backscatter (an indicator of fish and plankton density). The data were acquired in the summer of 2018 in three sampling periods (I01, 1-5 July; I02, 6-8 July; and I03, 9-13 July; see Methods for details of data set), and captured intense biophysical turbulence in every segment of nocturnal measurements. This allowed for an unprecedentedly detailed characterisation of biophysical turbulence, its mixing efficiency, and its biological underpinning.

Hydrographic and turbulence environments

The Ría's hydrographic setting varied notably during the measurement campaign, evolving from a downwelling to an upwelling circulation over the fortnight of observations (Figure 1a,b). In the first sampling period (I01), southerly, downwelling-favorable winds were dominant (Figure 1a) and thermal stratification was relatively weak (Figure 1b) as a result of the import into the embay-

ment of surface shelf waters with uniform temperature of ~17 ^{o}C. After 4 July, calm conditions prevailed, and the circulation pattern reversed (Extended Data Figure 2). During I02, relatively cold waters ($T \approx 13\,^{o}$C) upwelled into the Ría's deeper layers, giving rise to a stratified interface at ~20 m. The inflow of warmer and fresher waters produced an additional near-surface (< 10 m) stratified layer (Figure 1b). At the outset of I03, strong northerly winds led to an intensification of cold-water upwelling, which brought about a single highly-stratified layer.

The evolution of the Ría's turbulence environment bared little imprint from that of the hydrography, hinting at a non-physical origin of the turbulence. Thus, turbulent dissipation was recurrently enhanced over the entire water column every day after sunset and for a period of 5-6 hours (Figure 1c). This enhancement (termed night-time dissipation hereafter) was most striking in the embayment's interior layers (10 – 25 m), away from the direct influence of wind-induced and bottom boundary turbulence. Within this depth interval, night-time ε was elevated by 1-3 orders of magnitude above background daytime values of 10^{-9} – 10^{-8} W kg^{-1}, reaching 10^{-7} – 10^{-5} W kg^{-1} (Figure 1c, Extended Data Table 1). Background ε levels were higher during I01 (mean 1.22×10^{-7} W kg^{-1}) compared to I02 (1.71×10^{-8} W kg^{-1}) and I03 (2.17×10^{-8} W kg^{-1}). Night-time dissipation rates also decreased between I01 (mean 1.62×10^{-5} W kg^{-1}) and I02-I03 (1.96×10^{-6} and 0.82×10^{-6} W kg^{-1}, respectively).

Sources of turbulence

To assess the energy sources of the turbulence in the Ría, we first examine the extent to which geophysical factors may explain the measured dissipation patterns. Geophysical turbulence in density-stratified waters commonly occurs when the destabilizing effect of vertical gradients of horizontal velocity (shear, sh^2, see Methods) overcomes the stabilizing effect of the vertical density gradient (stratification, N^2). Shear instability and turbulence are predicted to develop for low,

subcritical values of the gradient Richardson number, $Ri_g = N^2/sh^2 < 1/4$ (ref. 27). In our observational record, episodes of high near-surface ε (Figure 1c) were associated with intensified winds in particular days (Figure 1a), suggesting a physical driving of those turbulent patches. However, the occurrence of unstable conditions below 10 m did not exhibit a day-night cycle, as would be expected if shear instabilities generated the recurrent events of night-time dissipation. Instead, subcritical values of Ri_g within the water column became progressively rarer over the course of the experiment, as stratification increased (Figure 1e). Unstable conditions were relatively frequent and widespread during downwelling (I01), but retreated to the upper and bottom boundary layers during upwelling (I02 and I03). This disassociation between the observed turbulence and shear instabilities is succinctly illustrated by the weak correlation between ε and Ri_g (Spearman $r = -0.14$, $p < 0.01$, Extended Data Figure 3), which endorses the notion that the night-time dissipation was sustained by a non-physical energy source.

A window into the nature of such source is provided by the distribution of volume backscattering strength (Sv), a metric of the occurrence of fish, recorded with a vessel-mounted echosounder. Sv was systematically enhanced at night (Figure 1f), in remarkable concurrence with elevated turbulent dissipation. The intensity of backscatter was highly correlated with ε for all the sampled backscattering frequencies (18-200 kHz, $r = 0.56 - 0.67$, $p < 0.01$, Extended Data Figure 3), suggesting that the night-time dissipation events were driven by fish aggregations. Consistent with this interpretation, high concentrations of European anchovy (*Engraulis encrasicolus*) eggs were detected in plankton net hauls that were performed every morning of the experiment and in the night of 8 July (Figure 2). Local spawning of the eggs is indicated by both sets of hauls. In most of the morning hauls, the majority of eggs presented an F2 development stage (indicative of a time elapsed since spawning of 4–14 hours), whereas the night-time haul (01:54 pm GMT) was dominated by freshly spawned eggs at stage F1 (corresponding to a time since spawning of < 4 hours). Note, though, that lack of fish sampling gear on board prevented us from obtaining direct evidence

of the presence of fish.

At any rate, the picture that emerges from the net samples is one of a nocturnal aggregation of anchovies for spawning being responsible for driving our observed episodes of night-time dissipation. This view is endorsed by the acoustic frequency response (FR) within the nocturnal turbulent patches, which was elevated at 18 kHz compared to higher frequencies (Extended Data Figure 4), as previously described for anchovy aggregations[28]. It is also advocated by previous reports of such aggregations inside the Rías of NW Iberia[29,30], which reveal spawning to occur between 19:00 and 6:00 GMT (peaking at midnight)[31], with a seasonal maximum in July-August[32]. Thus, in the following, we will consider these episodes of intense nocturnal dissipation as being triggered by biophysical turbulence, and daytime periods of weaker dissipation as being dominated by geophysical turbulence.

Efficiency of turbulent mixing

As intense as the night-time biophysical turbulence may have been, did it effect commensurately substantial mixing? To address this question, we next characterize the mixing intensity by examining the record of temperature microstructure. This shows that the nocturnal biophysical turbulence events were associated with elevated values of the small-scale temperature-gradient variance (Extended Data Figure 5), the rate of thermal variance dissipation (χ, Extended Data Figure 6a) and the rate of turbulent mixing of heat (quantified by the diffusivity K_T, Figure 1d). This mixing enhancement was most evident during I03 and I02, which exhibited a >10-fold increase in temperature-gradient variance above daytime levels over a broad wavenumber range (Extended Data Figure 5), as well as an amplification of K_T by two orders of magnitude (relative to daytime values of $K_T < 10^{-6}$ m^2 s^{-1}, Figure 1d). The mixing impact of biophysical turbulence was more muted during I01, for which daytime turbulence was more energetic than for I02-I03 (Figure 1d).

The mixing efficiency, defined here as the fraction of TKE converted to potential energy, is assessed for our entire data set by computing the flux Richardson number, $R_f = K_T N^2/(\varepsilon + K_T N^2)$, where $K_T N^2$ and ε are respectively evaluated from microstructure measurements of temperature gradient and shear. R_f varied by up to three orders of magnitude during our observational period, including episodes of both geophysical and biophysical turbulence (Figure 3a). Mixing efficiencies close to the canonical value of $R_f = 0.16$ for geophysical, shear-driven turbulence were observed in the uppermost 10 m (mean $R_f = 0.153$ [$0.150 - 0.156$] [95% confidence intervals]), where turbulence is energized directly by wind. Below the surface (10–25 m), the frequency distribution of R_f was centered at lower values (mode $R_f \lesssim 0.1$), with broadly similar distributions for daytime geophysical turbulence and night-time biophysical turbulence (Figure 3a). The R_f distribution for geophysical turbulence was slightly less negatively skewed, as values larger than the mode ($R_f \approx 0.1$) were more frequent than in the R_f distribution for biophysical turbulence. The average mixing efficiency during night-time biophysical turbulence events ($R_f = 0.067$ [$0.064 - 0.069$]) was smaller than, but not significantly different to, the average value of R_f for background geophysical turbulence in the same depth interval ($R_f = 0.088$ [$0.086 - 0.090$]). Our data thus demonstrates that, contrary to the common view at present[24], biophysical turbulence can be a comparably efficient mixing agent to geophysical turbulence.

Discussion

Our observations reveal a consistent occurrence of elevated night-time levels of biophysical turbulence (reaching rates of dissipation as high as $10^{-6} - 10^{-5}$ W kg^{-1}, or two orders of magnitude above daytime values) during a two-week stretch, providing compelling evidence that fish can generate intense turbulence over prolonged periods. This contrasts with the results of several past investigations, which found biophysical turbulence challenging to detect in the field[19,20,22]. There are, however, several threads of evidence to propose that the representativeness of our results tran-

scends the specific spatio-temporal context of our measurements. First, our observed dissipation rates are similar to those documented previously in migrating zooplankton and krill layers[17,33] and fish aggregations[23,24,34]. They also conform to predictions by empirical models of biophysical turbulence which, on the basis of the size and characteristics of the swimming organisms[13,20], predict a rate of TKE production by the observed aggregations of $\sim 10^{-6}$ W kg^{-1} (see Methods). Finally, the aggregating fish behaviour that was responsible for the intense biophysical turbulence in our data is a recurrent feature in coastal upwelling areas in NW Iberia[29] and elsewhere[35]. This is illustrated by measurements of acoustic backscatter acquired by a moored acoustic current profiler in our study area between 26 June and 19 July, which revealed an enhancement of backscatter at almost every night in that extended period (Extended Data Figure 7).

An important result of the present work pertains to the observation of intense biophysical turbulence with a mixing efficiency comparable to that of geophysical turbulence. This finding challenges expectations from several previous studies that pointed to a reduction in mixing efficiency, and in the rate of mixing itself, in association with biophysical turbulence[23,24]. A theoretical explanation for such reduction was provided by Visser[8], who concluded that biophysical turbulence must necessarily be inefficient because the most abundant swimming organisms (zooplankton and fish) are small, and so produce small turbulent eddies ($0.01 - 0.1$ m). As these overturns would not be sufficiently large to interact with buoyancy forces, they would not induce mixing, but would be rapidly destroyed by viscosity instead.

To unravel the discrepancy between Visser's argument and our results, we examine the relationship between the mixing efficiency (again, quantified by R_f) and a set of key turbulent parameters[36]. This entails projecting our data onto a space defined by the turbulent Reynolds (Re_T) and Froude (Fr_T) numbers[37] (Figure 3b). We approximate these two numbers by ratios of length scales that describe the competition between inertial, buoyancy and viscous forces in the fluid,

following Ivey and Imberger[37]. While this simplified approach has some formal limitations[38], these do not affect our analysis' findings (see discussion in Methods). The turbulent Reynolds number, computed here as $Re_T = (L_T/L_K)^{4/3}$, represents the ratio of the mean size of the energy-containing eddies (denoted by the Thorpe scale, L_T; see Methods) to the viscosity-dominated Kolmogorov scale (L_K), and measures the competition between inertia and viscosity. The turbulent Froude number, here defined as $Fr_T = (L_O/L_T)^{2/3}$, quantifies the size of the observed turbulent eddies relative to the buoyancy or Ozmidov scale ($L_O = (\varepsilon/N^3)^{1/2}$), at which turbulent eddies are strongly influenced by buoyancy[39]. Thus, efficient mixing is expected when $L_T \approx L_O$ ($Fr_T \approx 1$), such that eddies interact with buoyancy forces and transport mass across the mean density gradient, and when Re_T is sufficiently large ($Re_T \gtrsim 100$), such that overturning motions are not readily damped by viscosity before they induce mixing[40]. According to Visser[8], biophysical turbulence is characterized by $Fr_T \gg 1$ (i.e. $L_T \ll L_O$), such that $R_f \ll 0.16$.

Bin-averaging our observational estimates of R_f in Re_T - Fr_T space reveals that the mixing efficiency was maximal ($R_f \geq 0.16$) when $Re_T > 100 - 1000$ and $Fr_T \approx 1$ (Figure 3b), as expected[37,39]. These energetic conditions were only found in the surface layer (< 10 m) directly energized by the wind. During daytime, geophysical turbulence in the interior (10–25 m) was characterized by $Re_T < 100 - 1000$ and $Fr_T \approx 0.5$, which signal conditions under which turbulence is susceptible to suppression by buoyancy ($L_T > L_O$) and viscosity[40], such that the mixing efficiency might be curbed ($R_f \lesssim 0.1$). Night-time biophysical turbulence was more energetic ($Re_T \approx 1000$), and contained overturns smaller than the Ozmidov scale ($L_T < L_O$, $Fr_T > 1-2$). For the I01 sampling period, when relatively weak stratification ($N^2 \approx 2 \times 10^{-4}$ s^{-2}, Extended Data Table 1) and elevated ε resulted in enhanced $L_O \approx 1$ m and $Fr_T = 2.63$ (Extended Data Table 1), fish-induced eddies ($L_T \approx 10-20$ cm, in line with the typical adult anchovy size in our study area[41] of ~12 cm) may have been too small to act on the background stratification, and the locus of the data in Re_T - Fr_T space suggests a reduction of R_f. In contrast, for I02 and I03, L_O was smaller (~20 cm) owing

to a decrease in ε and a strengthening of stratification ($N^2 = 5 - 10 \times 10^{-4}$ s^{-2}), and approached the size of the fish-driven turbulent overturns ($Fr_T \gtrsim 1$). Under these circumstances, the locus of the data in Re_T - Fr_T space indicates that $R_f \approx 0.1$, i.e. in line with the mixing efficiency of geophysical turbulence. In summary, Visser's argument on the presumed inefficiency of biophysical turbulence does not hold in our observations because, contrary to the argument's assumptions, L_O and L_T are comparable in a large portion of our data set (Figure 4).

Laboratory experiments suggest that the condition, $L_O \sim L_T$, upon which efficient biomixing is contingent, is promoted by aggregations of swimmers, which can produce large, aggregation-scale turbulent eddies[15,42]. Conversely, our observations suggest an alternative route toward efficient biomixing via an increase in stratification, which reduces buoyancy length scales (i.e. L_O) to the point that they become comparable to turbulent eddy sizes, even if these are significantly smaller than the aggregation scale. Our work thus shows that, besides biological factors –the agitated behaviour of the anchovies while spawning may have also played a role[42]–, the mixing efficiency of biophysical turbulence is controlled by the background stratification facilitating the injection of fish-induced TKE at the required scales. This conclusion implies that, while biomixing might be inefficient within the main open-ocean pycnocline (where $L_O \approx 1$ m; refs.[8,11]), it is likely to be considerably more effective in environments with stronger stratification, e.g., in seasonal pycnoclines or coastal seas (Figure 4). Such proposition appears particularly plausible in coastal regions, where riverine freshwater sources, solar heating and upwelling often give rise to highly stratified conditions[43], and spawning aggregations of small pelagic fish (e.g., sardine, herring or anchovy) are especially abundant[35,41,44,45]. Hence, our results not only substantiate the prediction that fish aggregations can generate intense turbulent dissipation levels, comparable to storms[13], but also show that elevated stratification fosters the occurrence of efficient biomixing. This highlights the potential of biophysical turbulence to drive enhanced vertical exchanges in upper-ocean areas with a rich biota, in many of which (e.g., in strongly stratified coastal waters)

vertical turbulent transfers contribute to the supply of nutrients for plankton growth[46] or the ventilation of de-oxygenated waters[47]. Therefore, biomixing could contribute promote phytoplankton growth and to reduce low-oxygen stress for higher trophic levels. The role of biomixing in shaping the physical and biogeochemical properties of productive upper-ocean regions should thus be reassessed.

Correspondence Correspondence and requests for materials should be addressed to B.F.C. (email: b.fernandez-castro@soton.ac.uk, bieito.fernandez@uvigo.es).

Acknowledgements Funding for this work was provided by the Spanish Ministry of Economy and Innovation under the research project REMEDIOS (CTM2016-75451-C2-1-R) to BM. BFC was supported by the Spanish Ministry of Economy and Innovation through a Juan de La Cierva-Formación postdoctoral fellowship (FJCI-641 2015-25712) and by the European Union's Horizon 2020 research and innovation program under the Marie Skłodowska-Curie grant agreement No. 834330 (SO-CUP). EB was supported by a postgraduate fellowship (ED481A- 2019/288) from Xunta de Galicia, co-funded by FSE Galicia (2014-2020). AC was supported by a postgraduate fellowship FPI (BES-2017-080935) from the Spanish Ministry of Economy and Competitiveness. ACNG acknowledges the support of the Royal Society and the Wolfson Foundation. We thank all the participants in the REMEDIOS cruise, particularly the crew of the R/V Ramón Margalef for their support, and Pilar Rial, Isabel Ramilo and Marina Villamaña for their contribution to data collection. We are also thankful to Gerardo Casas for his assistance in counting and staging of anchovy eggs. We are especially grateful to Paloma Chouciño for her logistic support during the cruise and assistance with microstructure data processing. Sebastiano Piccoloraz and Óscar Sepúlveda Steiner contributed to the development of the microstructure processing functions. Claudia Ofelio designed the illustration in Figure 4. We are thankful to the three reviewers for their comments which helped to improve the manuscript.

Author contributions. BFC and BMC conceived the study. BMC led the cruise. BFC, EN, MG, EB, AC and BMC participated in the data collection. BFC, MP, EN and MG analysed the data. All the authors contributed to the scientific discussions and interpretation of the results. BFC, BMC and ACNG wrote the

manuscript with contributions from all the coauthors.

Competing Interests. The authors declare that they have no competing financial interests.

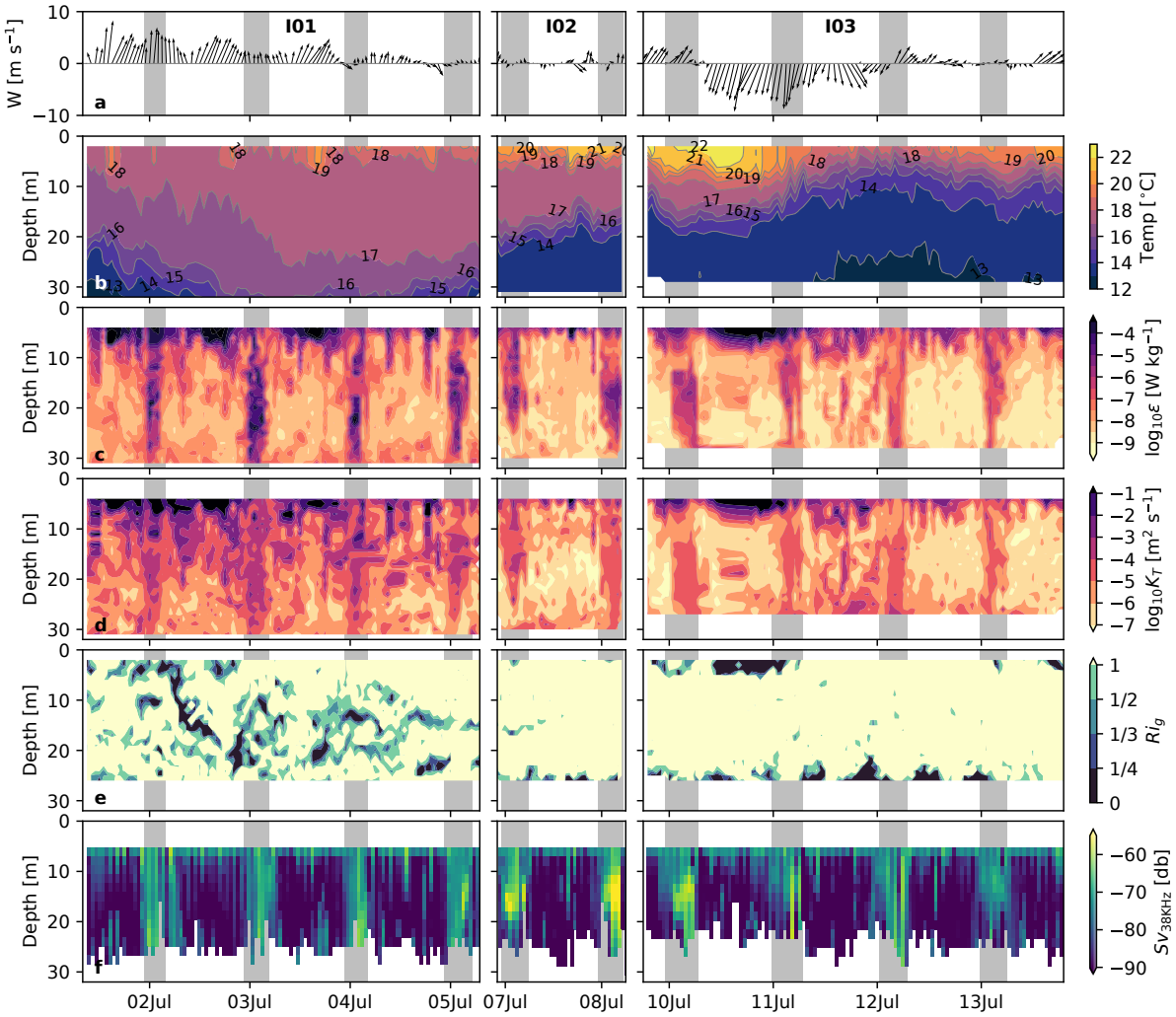

Figure 1: Hydrography, turbulence and mixing during the REMEDIOS survey. Time series of **a** local wind speed (W) and direction measured at Cape Udra (Extended Data Figure 1), and hourly-mean **b** temperature (Temp.), **c** turbulent kinetic energy dissipation rate (ε), **d** turbulent heat diffusivity (K_T), **e** gradient Richardson number (Ri_g), and **f** volume backscattering strength at 38 kHz (Sv), during the three sampling periods (I01, I02 and I03). Gray shading indicates night-time periods of biomixing. These periods were determined by inspection of the turbulent dissipation rate and volume backscattering strength records. The time axis is GMT time (local time = GMT + 2 hours). Note the use of logarithmic scale in panels **c, d**.

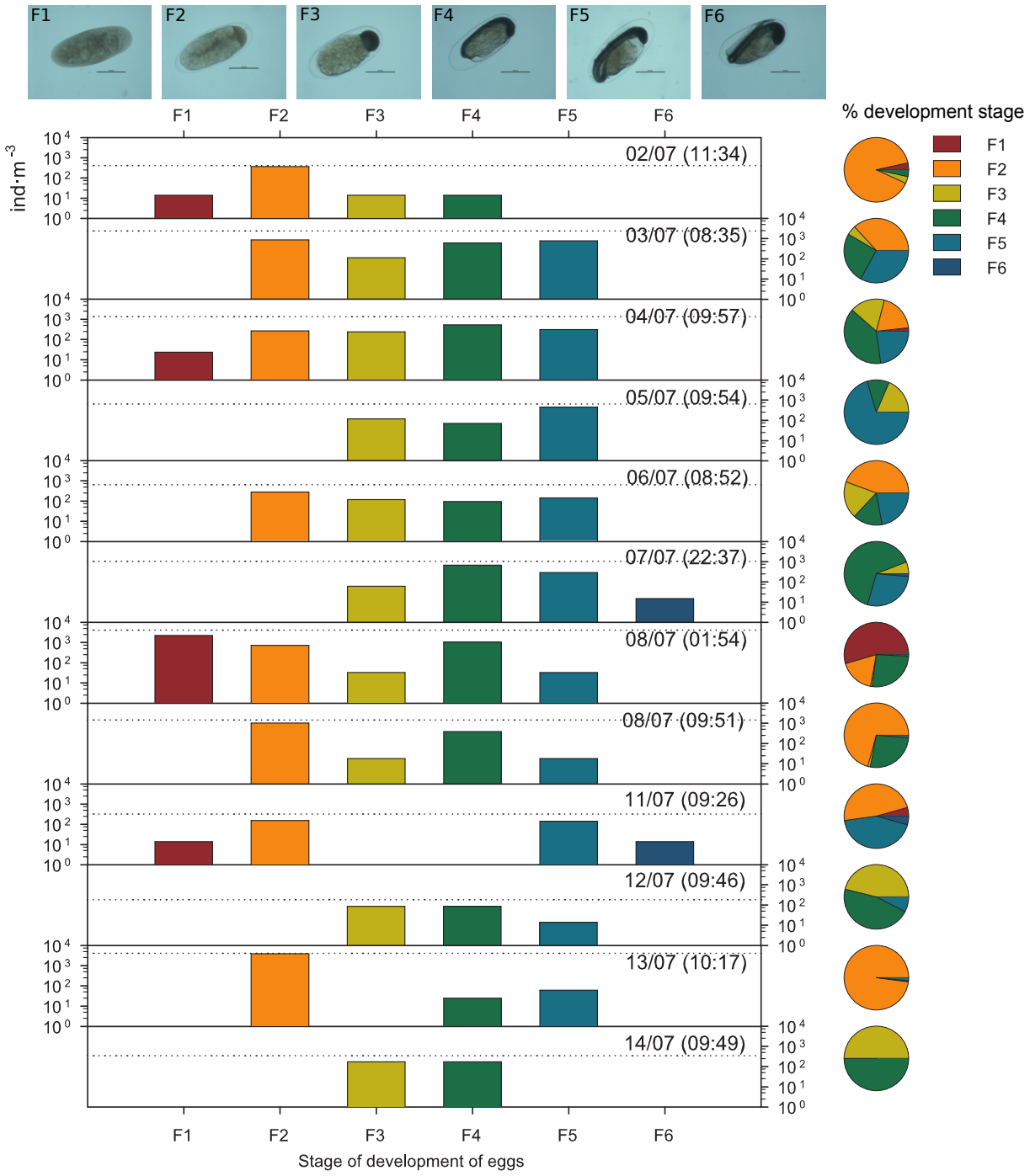

Figure 2: Anchovy egg concentration. Number of individuals per cubic metre (ind m^{-3}) at different development stages (F1 to F6, Extended Data Table 2) for the time series of plankton net hauls carried out at the sampling location. The date and hour of sampling (GMT), and the total number of eggs (horizontal dotted line) are shown in each bar plot. The y-axis is displayed in logarithmic scale. The pie charts indicate the percentages of eggs at the development stages considered, relative to the total number of eggs in each sample. The horizontal black line in each egg image (in the upper axis) denotes a length of 0.5 mm. Average elapsed times since spawning corresponding to the different development stages according to ref. [48] are: 0 hours (F1), 4.3 (F2), 14.3 (F3), 31.5 (F4), 48.3 (F5), and 59.3 (F6).

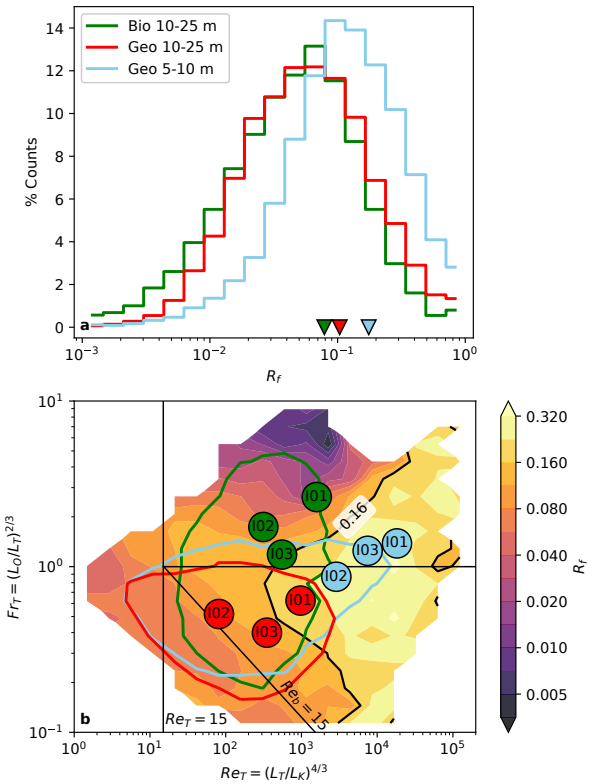

Figure 3: Mixing efficiency. a Frequency distribution of the flux Richardson number (R_f, a measure of the mixing efficiency) in the water column interior (10-25 m depth range) in periods dominated by biophysical turbulence (green) and in periods dominated by geophysical turbulence (red), and in the near-surface layer (5-10 m) for the full time series (light blue). Mean values are indicated with triangles. **b** Bin-averaged R_f in the Reynolds number – Froude number space ($Re_T - Fr_T$). The high-efficiency $Fr_T = 1$ (horizontal line), and molecular $Re_T = 15$ (vertical) and $Re_b = 15$ (oblique; $Re_b = (L_O/L_K)^{4/3}$) limits described by Ivey and Imberger[37] are shown as black lines. Mean values of Re_T and Fr_T are shown as circles for the three sampling periods (I01, I02 and I03), and for the different depth ranges. The green, red and light blue lines enclose bins in which frequency of occurrence exceeds 0.5% of the total counts for periods of biophysical turbulence (green, 10-25 m), and interior (red, 10-25 m) and near-surface (light blue, 5-10 m) geophysical turbulence.

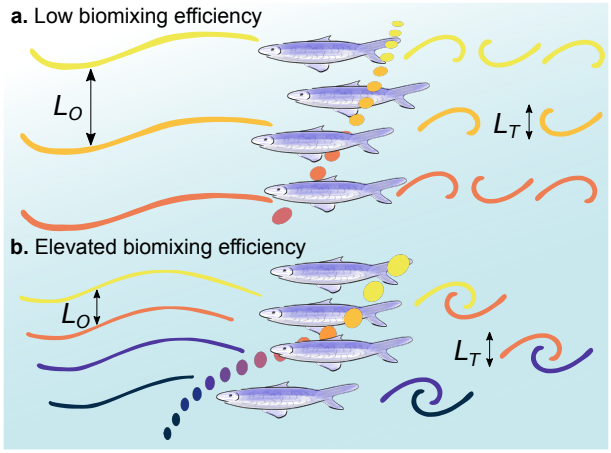

Figure 4: Schematic of the onset of efficient biomixing. Schematic representation of two scenarios of biophysical turbulence in contrasting levels of stratification, underpinning low (**a**) and elevated (**b**) mixing efficiency. In the first scenario, weak stratification (illustrated here by the colored lines and dots depicting layers of different temperature) results in a large buoyancy length scale (L_O) compared to the biologically-induced overturning scale (L_T). In this scenario turbulent eddies are dissipated by viscosity before producing significant mixing, and biophysical mixing is inefficient. Such conditions, mimicking those described by Visser[8] for the main open-ocean pycnocline, are broadly captured by our observations during I01. In the second scenario, representing conditions during I02-I03, L_O shrinks as stratification increases, becoming comparable to the overturning scale. This situation allows the turbulent eddies to interact with the temperature/density profile and transport heat/mass vertically before dissipating, thus leading to an increase in the efficiency of biomixing.

References

1. Thorpe, S. A. *The Turbulent Ocean* (Cambridge University Press, 2005).

2. Winters, K. B., Lombard, P. N., Riley, J. J. & D'Asaro, E. A. Available potential energy and mixing in density-stratified fluids. *J. Fluid Mech.* **289**, 115–128 (1995).

3. Osborn, T. R. Estimates of the local rate of vertical diffusion from dissipation measurements. *J. Phys. Oceanogr.* **10**, 83–89 (1980).

4. Oakey, N. S. Determination of the rate of dissipation of turbulent energy from simultaneous temperature and velocity shear microstructure measurements. *J. Phys. Ocean.* **12**, 256–271 (1982).

5. Smyth, W. D. & Moum, J. N. Marginal instability and deep cycle turbulence in the eastern equatorial Pacific Ocean. *Geophys. Res. Lett.* **40**, 6181–6185 (2013).

6. Gregg, M., D'Asaro, E., Riley, J. & Kunze, E. Mixing efficiency in the ocean. *Ann. Rev. Mar. Sci.* **10**, 443–473 (2017).

7. Monismith, S. G., Koseff, J. R. & White, B. L. Mixing efficiency in the presence of stratification: when is it constant? *Geophys. Res. Lett.* **45**, 5627–5634 (2018).

8. Visser, A. W. Biomixing of the oceans? *Science* **316**, 838–839 (2007).

9. Wunsch, C. & Ferrari, R. Vertical mixing, energy, and the general circulation of the oceans. *Annu. Rev. Fluid Mech.* **36**, 281–314 (2004).

10. Munk, W. H. Abyssal recipes. *Deep Sea Res.* **13**, 707–730 (1966).

11. Kunze, E. Biologically generated mixing in the ocean. *Ann. Rev. Mar. Sci.* **11**, 215–226 (2019).

12. Katija, K. Biogenic inputs to ocean mixing. *J. Exp. Biol.* **215**, 1040–1049 (2012).

13. Huntley, M. E. & Zhou, M. Influence of animals on turbulence in the sea. *Mar. Ecol. Prog. Ser.* **273**, 65–79 (2004).

14. Dewar, W. K. *et al.* Does the marine biosphere mix the ocean? *J. Mar. Res.* **64**, 541–561 (2006).

15. Houghton, I. A., Koseff, J. R., Monismith, S. G. & Dabiri, J. O. Vertically migrating swimmers generate aggregation-scale eddies in a stratified column. *Nature* **556**, 497–500 (2018).

16. Farmer, D. D., Crawford, G. B. & Osborn, T. R. Temperature and velocity microstructure caused by swimming fish. *Limnol. Oceanogr.* **32**, 978–983 (1987).

17. Kunze, E., Dower, J. F., Bevaridge, I., Bawey, R. & Bartlett, K. P. Observations of biologically generated turbulence in a coastal inlet. *Science* **313**, 1768–1770 (2006).

18. Rippeth, T. P., Gascoine, J. C., Green, J. A. M., Inall, M. E. & Palmer, M. R. Turbulent dissipation of coastal seas. eLetter in response to Kunze E., Dower J. F., Beveridge I., Dewey R., Bartlett K. P. (2006). Observations of biologically generated turbulence in a coastal inlet. *Science* **313** (2007).

19. Rousseau, S., Kunze, E., Dewey, R., Bartlett, K. & Dower, J. On turbulence production by swimming marine organisms in the open ocean and coastal waters. *J. Phys. Oceanogr.* **40**, 2107–2121 (2010).

20. Lorke, A. & Probst, W. N. In situ measurements of turbulence in fish shoals. *Limnol. Oceanogr.* **55**, 354–364 (2010).

21. Sato, M., Klymak, J. M., Kunze, E., Dewey, R. & Dower, J. F. Turbulence and internal waves in Patricia Bay, Saanich Inlet, British Columbia. *Cont. Shelf Res.* **85**, 153–167 (2014).

22. Simoncelli, S., Thackeray, S. J. & Wain, D. J. On biogenic turbulence production and mixing from vertically migrating zooplankton in lakes. *Aquat. Sci.* **80**, 35 (2018).

23. Gregg, M. C. & Horne, J. K. Turbulence, acoustic backscatter, and pelagic nekton in Monterey Bay. *J. Phys. Oceanogr.* **39**, 1097–1114 (2009).

24. Pujiana, K., Moum, J. N., Smyth, W. D. & Warner, S. J. Distinguishing ichthyogenic turbulence from geophysical turbulence. *J. Geophys. Res. Ocean.* **120**, 3792–3804 (2015).

25. Álvarez-Salgado, X., Gago, J., Míguez, B., Gilcoto, M. & Pérez, F. Surface waters of the NW Iberian Margin: upwelling on the shelf versus outwelling of upwelled waters from the Rías Baixas. *Estuar. Coast. Shelf Sci.* **51**, 821–837 (2000).

26. Pardo, P. C., Gilcoto, M. & Pérez, F. F. Short-time scale coupling between thermohaline and meteorological forcing in the Ría de Pontevedra. *Sci. Mar.* **65**, 229240 (2001).

27. Miles, J. Richardson's criterion for the stability of stratified shear flow. *Phys. Fluids* **29** (1986).

28. Park, J. *et al.* Frequency responses of anchovy schools in the South Sea of South Korea in spring and winter. *J. Korean Soc. Fish. Technol.* **52**, 111–120 (2016).

29. Ferreiro, M. J. *El ictioplancton de la ría de Vigo*. Phd thesis, Universidade de Santiago de Compostela (1985).

30. Motos, L., Uriarte, A. & Valencia, V. The spawning environment of the Bay of Biscay anchovy (Engraulis encrasicolus L.). *Sci. Mar.* **60**, 117–140 (1996).

31. Motos, L. Reproductive biology and fecundity of the Bay of Biscay anchovy population (Engraulis encrasicolus L.). *Sci. Mar.* **60**, 195–207 (1996).

32. Sola, A., Motos, L., Franco, C. & Lago de Lanzos, A. Seasonal occurrence of pelagic fish eggs and larvae in the Cantabrian Sea (VIIIc) and Galicia (IXa) from 1987 to 1989. *ICES C. M.* **H:25** (1990).

33. Simpson, J. H. *et al.* The annual cycle of energy input, modal excitation and physical plus biogenic turbulent dissipation in a temperate lake. *Water Resour. Res.* **57**, e2020WR029441 (2021).

34. Hooper, J. A., Baringer, M. O., St. Laurent, L. C., Dewar, W. K. & Nowacek, D. Dissipation processes in the Tongue of the Ocean. *J. Geophys. Res. Ocean.* **121**, 3159–3170 (2016).

35. Claramunt, G., Cubillos, L., Herrera, G. & Díaz, E. Spawning marker patterns of Engraulis ringens of northern Chile. *Fish. Res.* **219**, 105306 (2019).

36. Caulfield, C. Layering, instabilities, and mixing in turbulent stratified flows. *Annu. Rev. Fluid Mech.* **53** (2021).

37. Ivey, G. N. & Imberger, J. On the nature of turbulence in a stratified fluid. Part I: the energetics of mixing. *J. Phys. Oceanogr.* **21**, 650–658 (1991).

38. Mater, B. D., Schaad, S. M. & Venayagamoorthy, S. K. Relevance of the thorpe length scale in stably stratified turbulence. *Phys. Fluids* **25** (2013).

39. Mashayek, A. *et al.* Efficiency of turbulent mixing in the abyssal ocean circulation. *Geophys. Res. Lett.* **44**, 6296–6306 (2017).

40. Gargett, A. E., Osborn, T. R. & Nasmyth, P. W. Local isotropy and the decay of turbulence in a stratified fluid. *J. Fluid Mech.* **144**, 231 (1984).

41. Massé, J., Uriarte, A., Angélico, M. M. & Carrera, P. Pelagic survey series for sardine and anchovy in ICES Subareas 8 and 9 (WGACEGG) – Towards an ecosystem approach. *ICES Coop. Res. Rep.* 332 (2018).

42. Tanaka, M., Nagai, T., Okada, T. & Yamazaki, H. Measurement of sardine-generated turbulence in a large tank. *Mar. Ecol. Prog. Ser.* **571**, 207–220 (2017).

345 43. Largier, J. L. Upwelling bays: How coastal upwelling controls circulation, habitat, and pro-
346 ductivity in bays. *Ann. Rev. Mar. Sci.* **12**, 415–447 (2020).

347 44. Cury, P. *et al.* Small pelagics in upwelling systems: Patterns of interaction and structural
348 changes in 'wasp-waist' ecosystems. *ICES J. Mar. Sci.* **57**, 603–618 (2000).

349 45. Huse, G. A spatial approach to understanding herring population dynamics. *Can. J. Fish.*
350 *Aquat. Sci.* **73**, 177–188 (2016).

351 46. Sharples, J. *et al.* Phytoplankton distribution and survival in the thermocline. *Limnol.*
352 *Oceanogr.* **46**, 486–496 (2001).

353 47. Diaz, R. J. Overview of Hypoxia around the World. *J. Environ. Qual.* **30**, 275–281 (2001).

Methods

Sampling overview. The REMEDIOS sampling campaign was carried out off the Galician coast (NW Iberian Peninsula) between 29 June and 18 July 2018 on board of R/V Ramón Margalef (Extended Data Figure 1). Three intensive sampling time series were performed: I01 (2018.07.02 08:00 am to 2018.07.06 08:40 am), I02 (2018.07.07 10:07 pm to 2018.07.09 05:23 am), and I03 (2018.07.10 5:50 pm to 2018.07.14 7:30 pm) at station P2-Bueu, inside the Ría de Pontevedra (42.357^{o}N, -8.773^{o}E, mean depth 30 m). During these sampling periods, five casts were performed every half hour with a microstructure profiler (MSS[49]), resulting in a total number of 1658 profiles (~50 km of microstructure data). This sequence was interrupted every 6 hours for water collection with a Rosette. Water velocity profiles were continuously recorded with a bottom-moored acoustic Doppler current profiler (ADCP), and volume backscattering strength was registered with a hull-mounted echosounder.

Microstructure measurements. The MSS was equipped with two shear microstructure sensors (type PNS06) and a temperature microstructure sensor (type FP07), complemented with a high-accuracy CTD and an accelerometer to assess the instrument's vibration. The various channels were sampled at 1024 Hz, and the instrument was loose-tethered and operated in free-falling mode at a nominal vertical speed of 0.6–0.7 m s^{-1}. The dissipation rates of turbulent kinetic energy (ε) and thermal variance (χ) were calculated by integrating the vertical shear and vertical temperature-gradient spectra over half-overlapping segments of 2 m. The shear microstructure signal was de-noised for instrument vibration using the accelerometer signal[50]. A pseudo-shear signal was also derived from the accelerometer to assess ε contamination by instrument vibration. The temperature-gradient spectra were corrected for the FP07 time-response (τ = 12 m s^{-1}) with a double-pole function, previous to integration[51]. The shear spectra were integrated from a minimum wavenumber of 2 cycles per meter (cpm). The upper integration limit was estimated iteratively from an initial guess of 14 cpm until convergence to the Kolmogorov wavenumber

($k_c = \frac{1}{2\pi}\left(\varepsilon\nu^{-3}\right)^{1/4}$) was achieved. The upper cut-off was curtailed to a maximum value of 30 cpm, in order to avoid the spectral region where the spatial response of the shear probe becomes limiting and noise is introduced by instrument vibrations. The temperature gradient spectra were also integrated from 2 cpm. The upper integration limit in this case was chosen as the minimum of the following wavenumbers: the wavenumber at which the measured spectra becomes smaller than two times an empirical noise spectrum (see Extended Data Figure 5, Supplementary Figures 1, 2); the wavenumber at which the time-response correction is larger than a factor of 100; and a wavenumber corresponding to a frequency of 60 Hz. The missing variance at wavenumbers beyond the integration limits was estimated by assuming that the shear and temperature spectra respectively follow the empirical Nasmyth and Bachelor forms[52]. Prior to the missing-variance correction, ε values were corrected for the probe's spatial response using the polynomial factors given by the manufacturer[53]. Note that the variance correction can be substantial for high levels of dissipation (i.e. $\varepsilon > 10^{-6}$ W kg^{-1}), however, the measured spectra show excellent agreement with the empirical universal forms for intense turbulence over the resolved wavenumber range (Supplementary Figure 1), supporting the robustness of the estimation. This methodology is described in more detail elsewhere[54]. During night-time biomixing periods, fish impacts on the profiler were often apparent in the shear and pseudo-shear (accelerometer) records (Supplementary Figure 2). These data segments were manually identified and discarded from further analysis. Impacts were frequent during I01 (1772 of 2829 segments discarded), but rare during I02 (129 of 1866 segments discarded) and I03 (114 of 3378 segments discarded) (Extended Data Table 1).

Mixing characterization. The stability with respect to shear-driven turbulence was characterized with the gradient Richardson number, $Ri_g = N^2/sh^2$, where $N^2 = -g/\rho(\partial_z\rho)$ is the buoyancy frequency, with ρ as the potential density, and $sh^2 = (\partial_z u)^2 + (\partial_z v)^2$ is the squared vertical shear, with u and v as the zonal and meridional velocity components. The turbulent diffusivity for heat was calculated using the Osborn-Cox[55] relation as $K_T = 0.5\chi/(\partial_z T)^2$, where $\partial_z T$ is the back-

ground temperature gradient. Mixing efficiency was quantified with the flux Richardson number ($R_f = K_T N^2/(\varepsilon + K_T N^2)$), and the vertical size of turbulent overturns with the Thorpe length scale (L_T). L_T was computed by comparing the measured potential density with an adibatically resorted density profile[56]. Other relevant scales for turbulence are the Ozmidov ($L_O = (\varepsilon N^{-3})^{1/2}$) and the Kolmogorov ($L_K = (\nu^3 \varepsilon^{-1})^{1/4}$) length scales, where ν is the kinematic viscosity, $\sim 10^{-6}$ m^2 s^{-1}.

Acoustic backscatter and fish density. A Simrad EK80 echosounder operated the split-beam transducers of 18, 38, 70, 120 and 200 kHz at continuous wave mode with maximum pinging rate, registering 50 metres of data in the vertical. Pulse duration was set to 1 ms for all the frequencies, while the beam width was 11° for 18 kHz and 7° for higher frequencies. Transmitting power was 1600, 1600, 675, 225 and 135 W, respectively, for each frequency. The standard sphere calibration procedure was performed after the survey[57]. A mean volume backscattering coefficient (Sv, dB re 1 m^2 m^{-3}, dB hereafter) was averaged (in the linear domain) in bins of 2 metres by 30 minutes, after removing the 6 metres where ringing noise (remaining vibration of the echosounder while already listening) affected the 18 kHz echogram.

European anchovy eggs Sampling of *Engraulis encrasicolus* eggs was performed by means of oblique hauls from the surface down to 3 m above the bottom (~30 m depth) with a double-WP2 plankton net (HydroBios; 3.95 m^2 mouth area; 200 μm mesh-size), at a descending/ascending rate of 50/30 metres per minute and a trawling speed of 2 knots. Each net carried a mechanical flowmeter (General Oceanics) to estimate the volume of sampled water (between ca. 17 and 32 m^3). Collected samples were preserved with buffered formaldehyde (4% final concentration). Counting and definition of the development state of eggs were carried out with a stereoscopic binocular (Nikon SMZ-10). Sample aliquots of 20 mL, from a solution of 400 mL of the whole sample, were used for those purposes. To illustrate development state (Extended Data Table 2), microphotographs were taken with a stereoscopic binocular and dedicated image acquisition software (Nikon SMZ-1270 and NIS-Elements). Development state was classified in stages according

to morphological properties of the embryo[58]. The eggs collected during the survey were classified into 6 stages (F1 to F6), focusing on the characterization of development in the first 12 hours after spawning and considering a reference temperature of 17 ^{o}C (ref. [48]). Stages applied here (F1 to F6), their equivalence to the stages ('stageing') proposed in ref. [58] (I to XI), stage duration after spawning in hours (for 17 ^{o}C ambient temperature) and morphological characteristics of the embryo [from Table A1.3 of ref. [41]] are given in Extended Data Table 2.

Currents and continuous backscatter. A RD Instruments ADCP (300 kHz) was bottom-moored looking upwards in station P2-Bueu before the start of the cruise (2018.06.26), and was recovered after the end of the cruise (2018.07.19) from R/V Kraken. The three-dimensional current was recorded every 5 minutes as the average of 120 individual pings in 70 layers of 0.5 m, spanning the water column from 4 m above the bottom to the surface. ADCP backscatter was converted to volume backscattering strength (Sv, dB) following refs.[60,61].

TKE production by anchovy aggregations. TKE production by the anchovy aggregations was estimated as $P_{\mathrm{TKE}} = 0.072/3\, nU^{14/5}L^{9/5}\nu^{0.2} \approx 10^{-6}$ W kg^{-1}, following refs.[13,20], where $\nu \approx 1 \times 10^{-6}$ m^2 s^{-1} is the molecular viscosity of seawater. A characteristic fish size of $L = 12$ cm (corresponding to the modal size of 1-year-old anchovy adults[41]) and a swimming speed of $U \approx 36$ cm s^{-1} (equivalent to three body lengths per second[64]) were used in the calculation. Fish concentration in the aggregation (n, individuals per m^3) was calculated using the relationship between target strength for a given species (TS) and the observed volume backscattering (Sv = TS + $10\log_{10}(n)$). Using the target strength at 38 kHz employed for the PELACUS surveys in this area[41] ($TS = 20 \times \log_{10}(L) - 72.6 = -51.02$), the recorded mean Sv in the shoal at 38 kHz (-53.63 dB for I02) would convert into a concentration of $n = 0.5$ individuals per m^3.

Mixing efficiency in the Re_T–Fr_T diagram In order to synthesize the variability of the flux Richardson number (R_f, a measure of the mixing efficiency) in our cruise measurements, and

rationalize the relatively high efficiency diagnosed for biophysical mixing, we placed our data in a Reynolds-Froude (Re_T-Fr_T) numbers diagram. Projection onto Re_T-Fr_T space is useful to describe the balance of forces in a turbulent fluid which, in turn, underpins the efficiency of mixing. The state-of-the-art profiling instruments enabling quantification of turbulence in natural waters, such as the MSS employed in this study, do not directly measure Re_T and Fr_T. Thus, following common practice in ocean turbulence works[37], we approximate these quantities using turbulence length scales that can be directly assessed from the measurements: the Ozmidov ($L_O = (\varepsilon N^{-3})^{1/2}$), Kolmogorov ($L_K = (\nu^3 \varepsilon^{-1})^{1/4}$) and Thorpe ($L_T$, see Methods) length scales, such that:

$$Re_T = \left(\frac{L_T}{L_K}\right)^{4/3} \tag{1}$$

and

$$Fr_T = \left(\frac{L_O}{L_T}\right)^{2/3}. \tag{2}$$

Recent evidence from direct numerical simulations[38] (DNS) suggests that these approximate definitions of Re_T and Fr_T are only valid in a weakly-stratified regime, defined by $L_T < L_O$. According to these authors, the length scale dependency of Re_T and Fr_T differs for a highly-stratified regime ($L_T > L_O$), which would apply to a significant portion of our data. In such a regime,

$$Re_T = \left(\frac{L_T^3}{L_O^2 L_K}\right)^{4/3} \tag{3}$$

and

$$Fr_T = \left(\frac{L_O}{L_T}\right)^{2}. \tag{4}$$

Here, we assess the impact that this regime shift has for our conclusions by re-calculating Re_T and Fr_T using equations 3-4. The results (Supplementary Figure 3) show that the diagram is "stretched" relative to Figure 3b, owing to the stronger power dependencies of the scaling func-

tions in the highly-stratified regime. However, the key patterns supporting our findings remain unchanged.

Specifically, biophysical turbulence (green contour) spans a wide range of Fr_T values, with some data points intruding into an area with $Fr_T > 1$ and very low mixing efficiency, but with many others located closer to $Fr_T = 1$ (and even $Fr_T < 1$) where mixing efficiency is higher. In contrast, interior geophysical turbulence (red contours) appears in an area with $Fr_T < 1$ and possible turbulence suppression by buoyancy forces (around the oblique line representing $Re_b \approx 10$, where buoyancy forces suppress mixing). Geophysical turbulence in the wind-influenced surface layer displays data points in an energetic region of higher efficiency. In summary, although the shape of the diagram is slightly different, our key conclusions –i.e. that biomixing is occasionally suppressed because $Fr_T > 1$ (particularly during I01), but not as stronger stratification reduces Fr_T during I02-I03; and that geophysical turbulence in the interior is partly suppressed by buoyancy, thereby making the efficiency of biophysical and geophysical mixing comparable– hold irrespectively of the approach chosen to estimate the turbulence parameters.

Data availability. The data that support the findings of this study are available at a Zenodo repository, `doi:10.5281/zenodo.5559023`.

Code availability. The scripts used for microstructure data processing are freely available at `https://github.com/bieitofernandez/MSS_processing`

References

48. Ibaibarriaga, L. *et al.* Characterization of stage-classified biological processes using multinomial models: A case study of anchovy (Engraulis encrasicolus) eggs in the Bay of Biscay. *Can. J. Fish. Aquat. Sci.* **64**, 539–553 (2007).

493 49. Prandke, H. & Stips, A. Test measurements with an operational microstructure-turbulence
494 profiler: Detection limit of dissipation rates. *Aquat. Sci.* **60**, 191–209 (1998).

495 50. Levine, E. R. & Lueck, R. G. Turbulence measurement from an autonomous underwater
496 vehicle. *J. Atmos. Ocean. Technol.* **16**, 1533–1544 (1999).

497 51. Gregg, M. C. Uncertainties and limitations in measuring ϵ and χ(T). *J. Atmos. Ocean. Technol.*
498 **16**, 1483–1490 (1999).

499 52. Batchelor, G. K., Howells, I. D. & Townsend, A. A. Small-scale variation of convected quan-
500 tities like temperature in turbulent fluid: Part 1. General discussion and the case of small
501 conductivity. *J. Fluid Mech.* **5**, 113–133 (1959).

502 53. Stips, A. & Prandke, H. Recommended algorithm for dissipation rate calculation within
503 PROVESS 1–17 (2000).

504 54. Piccolroaz, S., Fernández-Castro, B., Toffolon, M. & Dijkstra, H. A. A multi-site, year-round
505 turbulence microstructure atlas for the deep perialpine Lake Garda. *Sci. Data* **8**, 1–20 (2021).

506 55. Osborn, T. R. & Cox, C. S. Oceanic fine structure. *Geophys. Fluid Dyn.* **3**, 321–345 (1972).

507 56. Thorpe, S. A. Turbulence and mixing in a Scottish Loch. *Phil. Trans. R. Soc. Lond. A* **286**,
508 125–181 (1977).

509 57. Demer, D. A. *et al.* Calibration of acoustic instruments. *ICES Coop. Res. Rep.* **326** (2015).

510 58. Moser, M. H. & Ahlstrom, E. H. Staging anchovy of eggs. In *An egg Prod. method Estim.*
511 *spawning biomass pelagic fish Appl. to North. Anchovy, Engraulis mordax. NOAA Tech. Rep.*
512 *NMFS 36*, 37–42 (1985).

513 59. Massé, J., Uriarte, A., Angélico, M. M. & Carrera, P. Pelagic survey series for sardine and
514 anchovy in ICES Subareas 8 and 9 (WGACEGG) – Towards an ecosystem approach. *ICES*
515 *Coop. Res. Rep.* 332 (2018).

60. Deines, K. L. Backscatter estimation using broadband acoustic Doppler current profilers. *Proc. IEEE Work. Conf. Curr. Meas.* 249–253 (1999).

61. Mullison, J. Backscatter Estimation Using Broadband Acoustic Doppler Current Profilers - Updated. *Appl. Note FSA-031* (2017).

62. Huntley, M. E. & Zhou, M. Influence of animals on turbulence in the sea. *Mar. Ecol. Prog. Ser.* **273**, 65–79 (2004).

63. Lorke, A. & Probst, W. N. In situ measurements of turbulence in fish shoals. *Limnol. Oceanogr.* **55**, 354–364 (2010).

64. Peraltilla, S. & Bertrand, S. In situ measurements of the speed of Peruvian anchovy schools. *Fish. Res.* **149**, 92–94 (2014).

65. Ivey, G. N. & Imberger, J. On the nature of turbulence in a stratified fluid. Part I: the energetics of mixing. *J. Phys. Oceanogr.* **21**, 650–658 (1991).

66. Mater, B. D., Schaad, S. M. & Venayagamoorthy, S. K. Relevance of the thorpe length scale in stably stratified turbulence. *Phys. Fluids* **25** (2013).

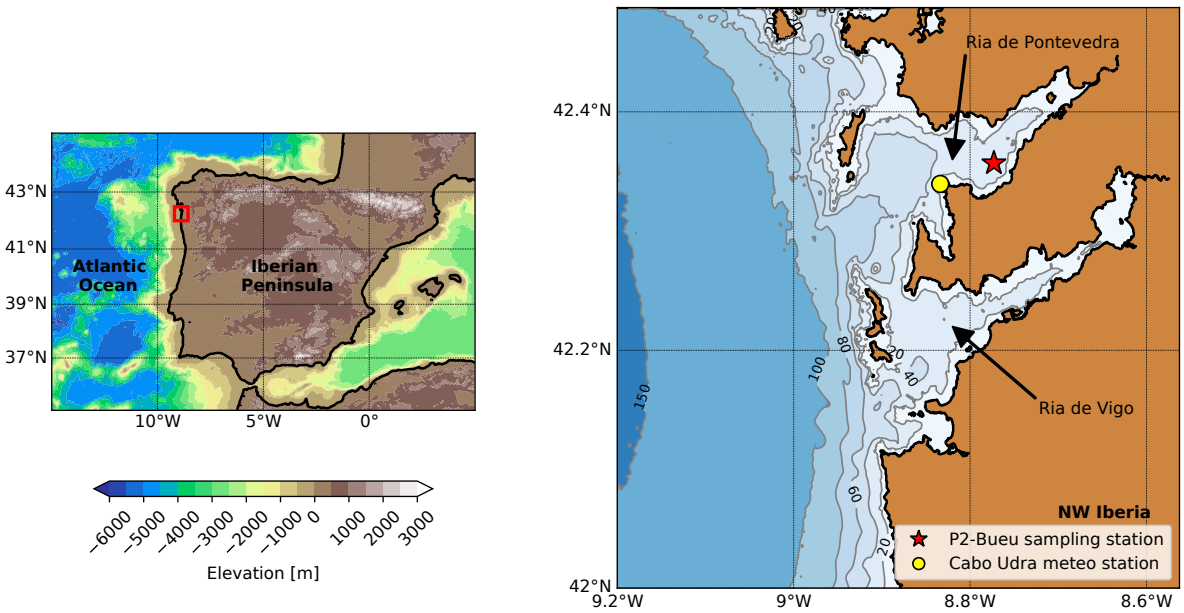

Extended Data Figure 1: Location of survey. Map of the location of the REMEDIOS sampling station P2-Bueu (red star, 42.357°N, -8.773°W, mean depth 30 m) in the Ría de Pontevedra (off the Galician coast, NW Iberian Peninsula). The location of the closest Meteogalicia (`www.meteogalicia.gal`) meteorological station (Cape Udra, 42.340°N, -8.884°E) is also shown.

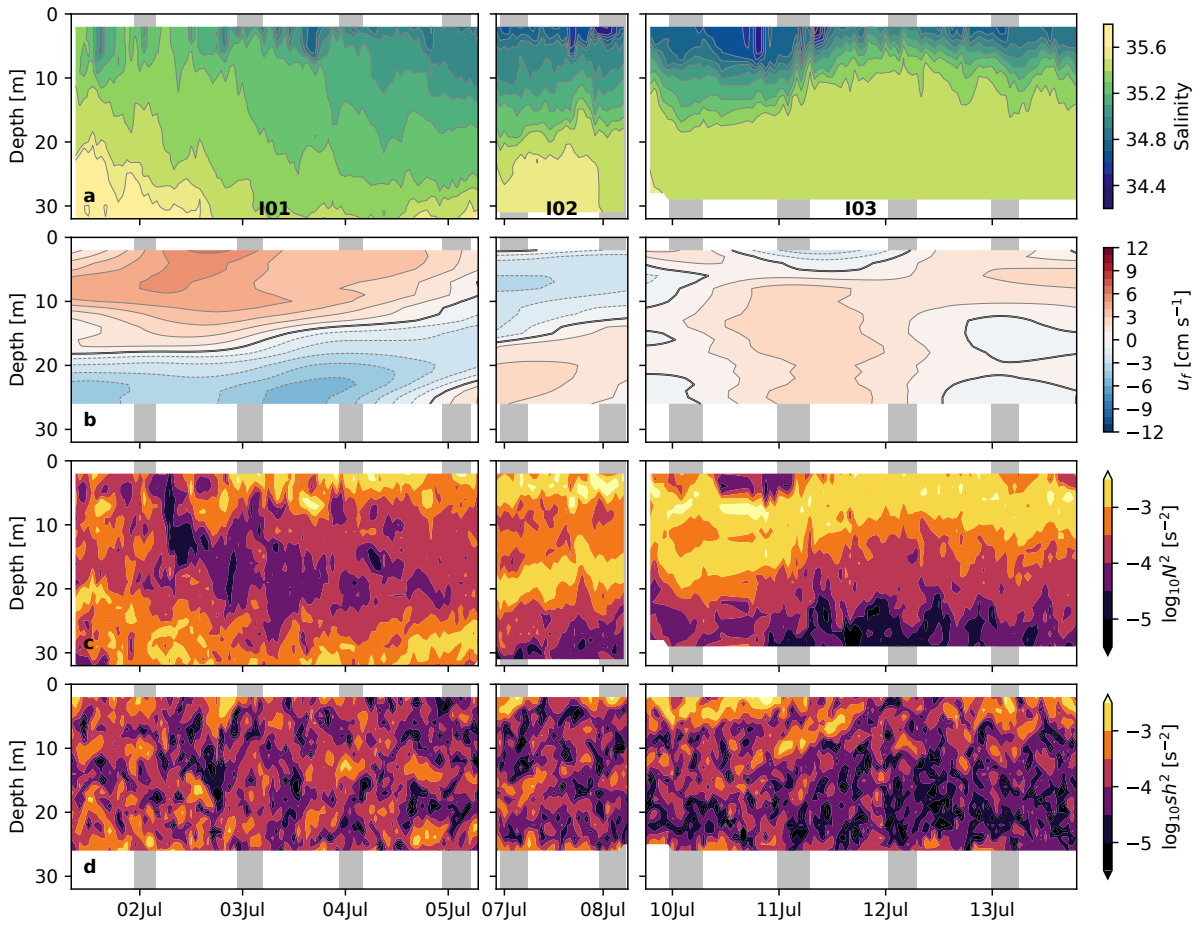

Extended Data Figure 2: Hydrographic setting. Hourly mean time series of **a** salinity, **b** de-tided eastward velocity (u), **c** squared buoyancy frequency (N^2), and **d** squared vertical shear of horizontal velocity (sh^2) during the three sampling periods (I01, I02 and I03). Gray shading indicates night-time biomixing events. These periods were determined by inspection of the turbulent dissipation rate and volume backscattering strength records. De-tided residual velocity was calculated with a 24/25/24 h Godin filter. Positive eastward velocity imports offshore waters into the Ría, and negative westward velocity exports onshore waters out of the Ría. Note the use of logarithmic scale in panels **c** and **d**.

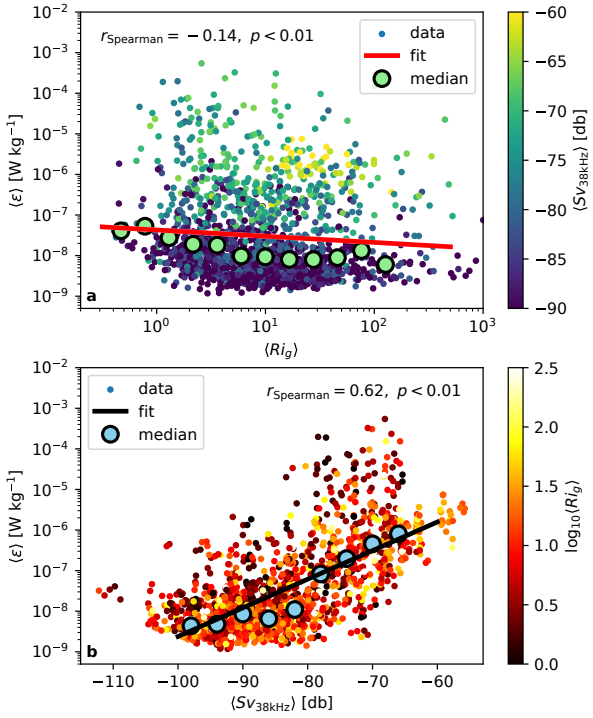

Extended Data Figure 3: Sources of turbulence. Depth-averaged (10–25 m) ε vs. **a** depth-averaged Ri_g and **b** 38 KHz volume backscattering strength (Sv). ε median values in bins of Ri_g and $Sv_{38\text{kHz}}$ are indicated as large circles. Linear fits in logarithmic scale and Spearman correlation coefficients are shown. The color scale represents $Sv_{38\text{kHz}}$ and Ri_g in panels **a** and **b**, respectively.

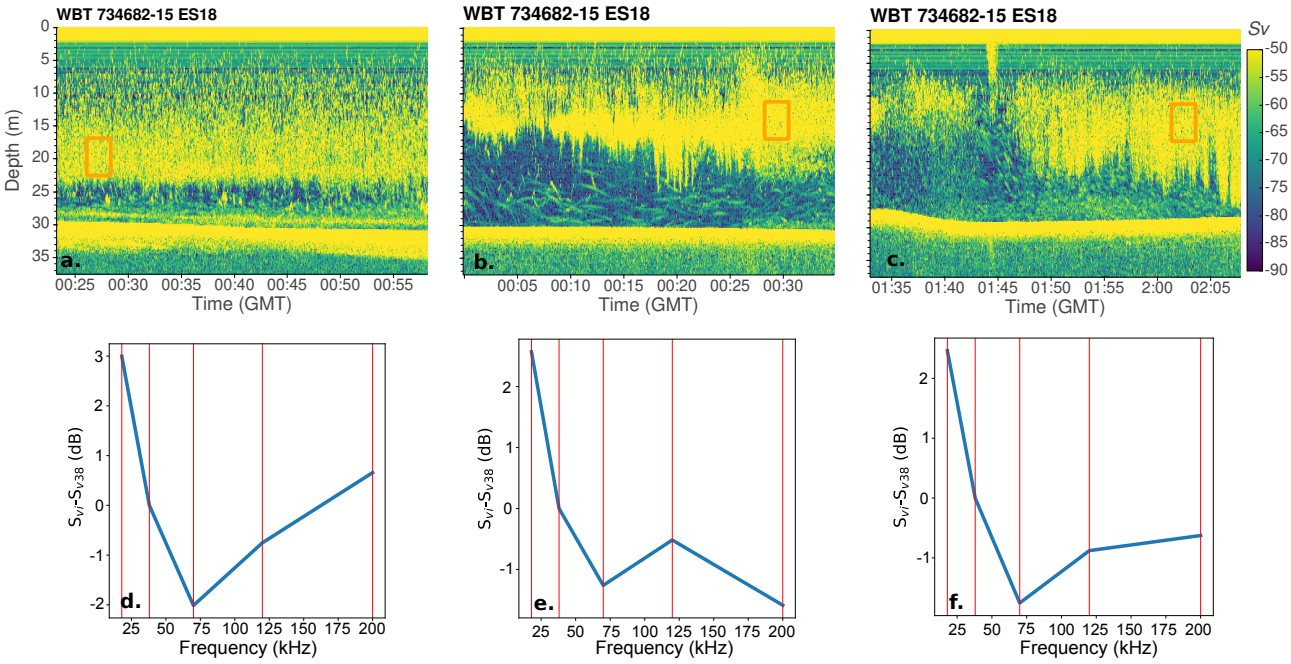

Extended Data Figure 4: Acoustic backscatter frequency response. Three examples of night-time echograms at 18 KHz, recorded during sampling periods I01 (**a**, 4 July), I02 (**b**, 8 July) and I03 (**c**, 12 July). Panels **d**-**f** show the mean frequency response (Sv at each frequency minus Sv at 38 kHz) for the region enclosed by the orange squares in panels **a**-**c**.

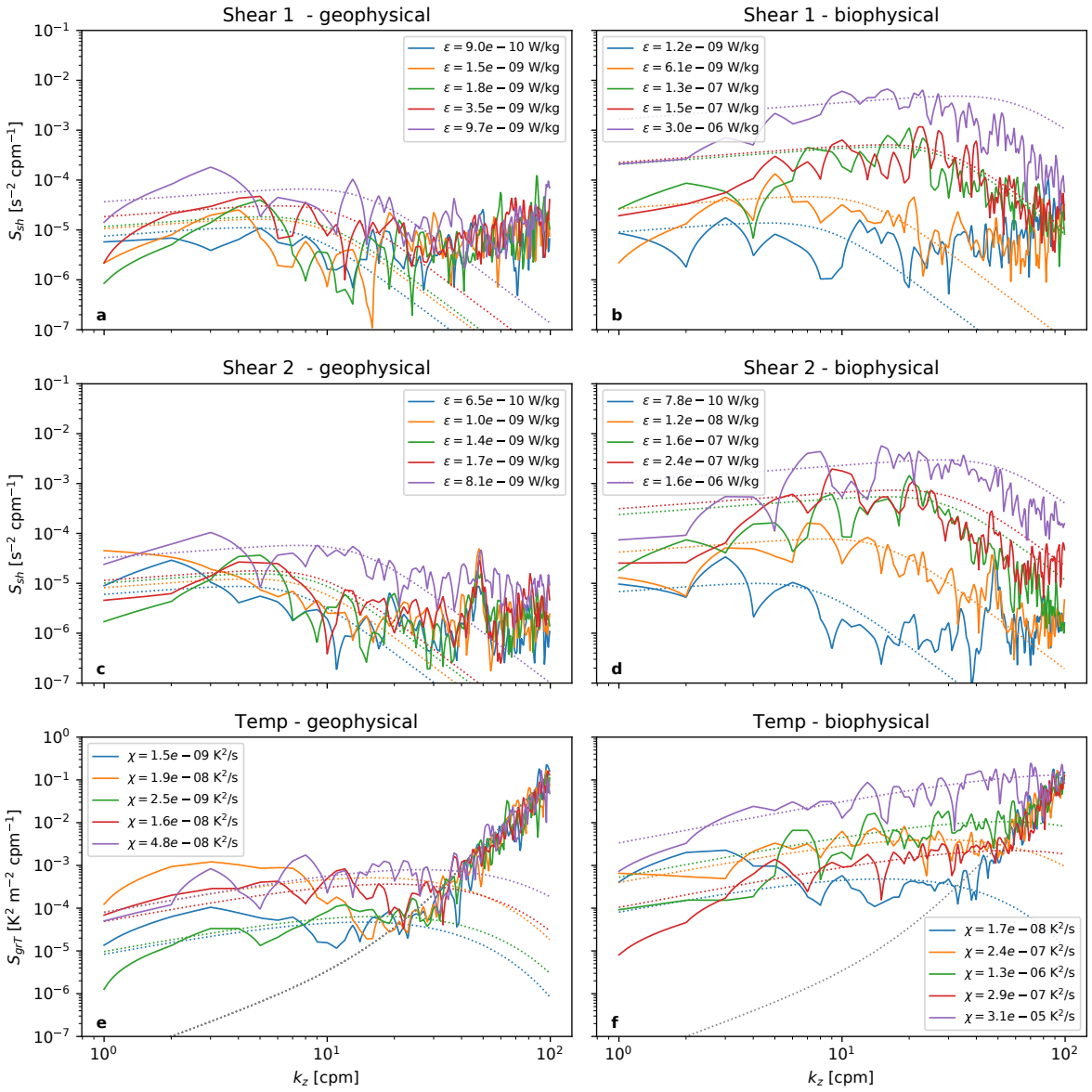

Extended Data Figure 5: Microstructure spectra. Randomly selected wavenumber (k_z, units: cycles per meter, cpm) spectra of vertical shear (**a-d**) and temperature gradient (**e, f**) microstructure between 10 and 25 m depth, during the third sampling period (I03). Periods dominated by geophysical turbulence are shown in the left column, and those dominated by biophysical turbulence (gray shading in Figure 1), in the right column. The corresponding universal spectra are indicated by dotted coloured lines, and the computed dissipation rates of turbulent kinetic energy (ε) and thermal variance (χ) are reported. Spectra recorded with the two shear sensors over the same portion of the water column are shown **a, b** and **c, d**, respectively. Empirical spectra of thermistor noise are represented by the gray dotted line **e,f** .

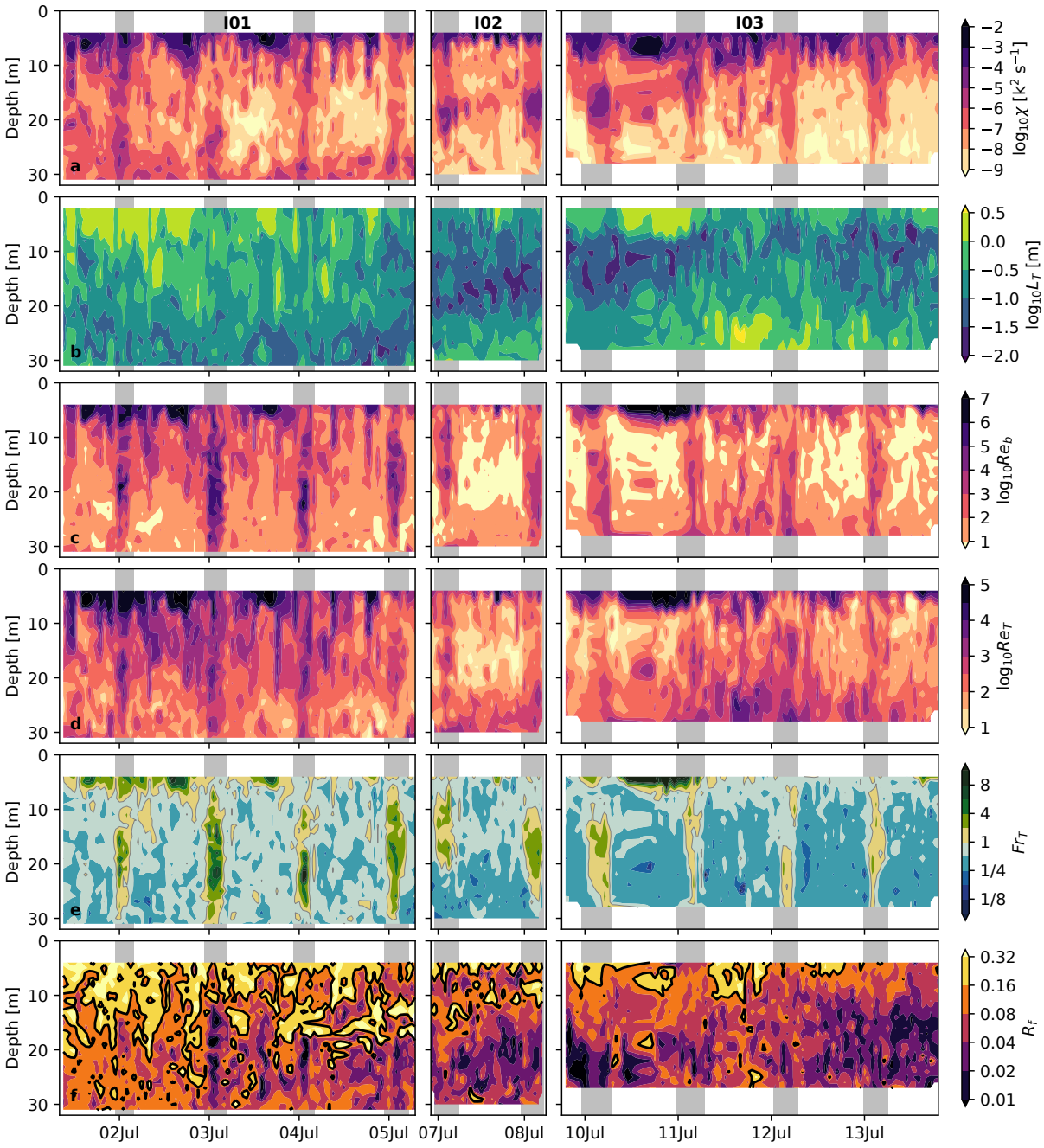

Extended Data Figure 6: Turbulence and mixing parameters. Time series of hourly mean **a** rate of dissipation of thermal variance (χ), **b** Thorpe scale (L_T), **c** buoyancy Reynolds number (Re_b), **d** turbulent Reynolds number (Re_T), **d** turbulent Froude number (Fr_T), and **f** flux Richardson number (R_f, a proxi for mixing efficiency) during the three sampling periods (I01, I02 and I03). Gray shading indicates night-time biomixing. Note the use of a logarithmic scale in all panels.

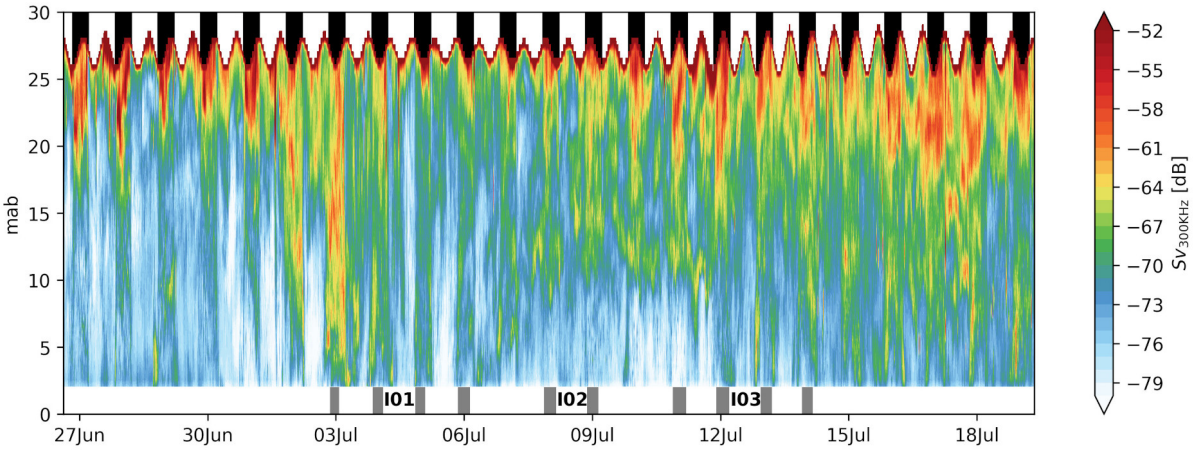

Extended Data Figure 7: ADCP backscatter. Time series of volume backscattering strength (Sv, dB) measured with a 300 KHz bottom-moored ADCP. Nights and biomixing events during the sampling periods (I01, I02 and I03) are indicated with black and gray shading, respectively.

Extended Data Table 1: Mean turbulent properties. Mean values [95% confidence intervals in brackets], and/or median values (†) for the three sampling periods (I01, I02 and I03) and for times of biophysical and geophysical turbulence. Unless indicated, the averaging was performed over the 10–25 m depth range. The number of segments in which turbulent quantities were calculated, and were unaffected (n_{good}) or affected (n_{impatcs}) by impacts against the instrument, are indicated. The affected data were discarded and not used for computing averages. N^2 is the buoyancy frequency (a measure of stratification); sh^2, the vertical shear of the horizontal velocity; $Ri_g = N^2/sh^2$, the gradient Richardson number; ε the turbulent kinetic energy dissipation rate; χ, the thermal variance dissipation rate; K_T, the turbulent heat diffusivity; R_f the flux Richardson number or mixing efficiency; L_T, the Thorpe scale; L_O the Ozmidov scale; Fr_T, the turbulent Froude number; Re_T the turbulent Reynolds number; and Re_b the buoyancy Reynolds number.

	I01		**I02**		**I03**	
	Geophysical	Biophysical	Geophysical	Biophysical	Geophysical	Biophysical
n_{good} (n_{impacts})	8517 (0)	1772 (1057)	2573 (0)	1737 (129)	7531 (0)	3264 (114)
N^2 [s^{-2}]	$2.15\ [2.10 - 2.21] \times 10^{-4}$	$2.00\ [1.93 - 2.1] \times 10^{-4}$	$7.73\ [7.44 - 8.07] \times 10^{-4}$	$7.79\ [7.37 - 8.11] \times 10^{-4}$	$4.59\ [4.45 - 4.72] \times 10^{-4}$	$5.11\ [4.92 - 5.32] \times 10^{-4}$
sh^2 [s^{-2}]	$2.22\ [2.16 - 2.28] \times 10^{-4}$	$2.47\ [2.38 - 2.59] \times 10^{-4}$	$1.85\ [1.47 - 1.67] \times 10^{-4}$	$1.68\ [1.58 - 1.78] \times 10^{-4}$	$1.30\ [1.24 - 1.38] \times 10^{-4}$	$1.44\ [1.38 - 1.54] \times 10^{-4}$
Ri_g	$1.15^{\dagger}$	1.03	6.43	5.60	4.3	3.7
ε [W kg^{-1}]	$1.22\ [0.83 - 2.27] \times 10^{-7}$ 6.52×10^{-9} †	$1.62\ [1.14 - 2.59] \times 10^{-5}$ 8.80×10^{-8}	$1.71\ [1.18 - 2.86] \times 10^{-8}$ 3.35×10^{-9}	$1.96\ [1.50 - 2.43] \times 10^{-6}$ 7.73×10^{-8}	$2.17\ [1.83 - 2.70] \times 10^{-8}$ 2.18×10^{-9}	$0.82\ [0.55 - 1.41] \times 10^{-6}$ 4.25×10^{-8}
χ [K^2 s^{-1}]	$1.19\ [0.90 - 1.74] \times 10^{-6}$ 1.36×10^{-8} †	$1.73\ [1.30 - 2.41] \times 10^{-6}$ 8.64×10^{-8}	$4.38\ [2.44 - 8.90] \times 10^{-7}$ 1.37×10^{-8}	$1.10\ [0.94 - 1.42] \times 10^{-5}$ 3.41×10^{-7}	$5.40\ [3.98 - 8.76] \times 10^{-7}$ 5.80×10^{-9}	$4.23\ [3.69 - 5.09] \times 10^{-6}$ 1.50×10^{-7}
K_T [m^2 s^{-1}]	$1.30\ [0.63 - 2.76] \times 10^{-3}$ 4.85×10^{-6} †	$1.30\ [0.51 - 3.03] \times 10^{-3}$ 3.79×10^{-5}	$1.55\ [0.63 - 3.99] \times 10^{-5}$ 2.61×10^{-7}	$1.58\ [0.75 - 5.28] \times 10^{-4}$ 1.33×10^{-5}	$1.39\ [1.12 - 1.92] \times 10^{-5}$ 3.08×10^{-7}	$3.52\ [3.10 - 4.37] \times 10^{-5}$ 7.33×10^{-6}
R_f	0.137 [0.133 – 0.141]	0.092 [0.083 – 0.099]	0.068 [0.064 – 0.073]	0.081 [0.075 – 0.087]	0.053 [0.052 – 0.054]	0.052 [0.050 – 0.055]
L_T [m]	0.342 [0.333 – 0.350]	0.235 [0.225 – 0.245]	0.099 [0.093 – 0.103]	0.115 [0.110 – 0.123]	0.283 [0.273 – 0.292]	0.222 [0.212 – 0.230]
L_O [m]	0.195 [0.187 – 0.210]	1.35 [1.20 – 1.85]	0.028 [0.027 – 0.032]	0.23 [0.20 – 0.26]	0.058 [0.0558 – 0.062]	0.226 [0.214 – 0.240]
Fr_T	0.63 [0.62 – 0.64]	2.63 [2.48 – 2.91]	0.52 [0.51 – 0.53]	1.76 [1.66 – 1.88]	0.40 [0.400 – 0.41]	1.19 [1.14 – 1.23]
Re_T	1093 [1009 – 1205]	1716 [1482 – 2300]	85 [78 – 94]	321 [290 – 370]	343 [320 – 365]	548 [510 – 586]
Re_b	1961 [1271 – 3462]	160189 [102140 – 271970]	57 [31 – 141]	4002 [2828 – 5677]	113 [95 – 149]	1699 [1454 – 2079]

Extended Data Table 2: Anchovy development stages. Development stages of the European anchovy (*Engraulis encrasicolus*) eggs considered in the present work (F1 to F6), equivalence with the stages proposed in ref. [58] (Stageing) (I to XI), elapsed time since spawning according to ref. [48] for a reference ambient temperature of 17°C, description of the development of the embryo, according to Table A1.3 from ref. [41], and images of development stages (F1 to F6) (the bar inserted in the pictures is 0.5 mm length)

Stage	Stageing	Elapsed time [hours]	Description	Images
F1	I	0	Cell division has not begun. The cytoplasm of the single cell appears as a clear hemisphere at one pole, although may be displace to other locations. Unfertilized eggs are included in this stage.	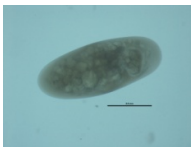
F2	II	4.3	Cell division starts. The blastodisc has a mulberry-like appearance. Blastula cells are very small, but it is possible to distinguish them.	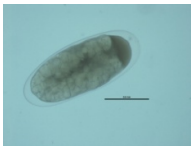
F3	III	14.3	The eggs have appearance of tissue rather than a collection of individual cells. The segmentation cavity is visible. The blastodermal cap is $\leq 1/3$ of the yolk mass.	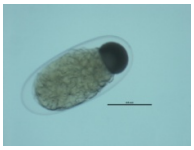
F4	IV-VI	31.5	The blastodermal cap is $> 1/3$ of the yolk mass. There is a rapid differentiation at this stage. At the end of this stage the angle between the tail and the yolk is $\geq 90°$	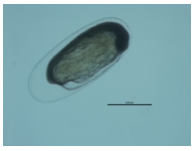
F5	VII-IX	48.3	The tip of the tail is free from the yolk. At the end of this stage, the curvature of the tail is evident and the gut is apparent along the ventral surface of the tail.	
F6	X-XI	59.3	The free portion of the tail is considered to extend from the body and not from the find-fold. The tail length is $\geq 3/4$ of the yolk-sac. At the end of this stage hatching takes place.